



SRTTU

Journal of Computational and Applied Research
in Mechanical Engineering

jcarme.sru.ac.ir

JCARME

ISSN: 2228-7922

Research paper

Development of a numerical tool for ingestion modeling and extracting rim seal performance map for a gas turbine network

Samaneh Hajikhani^a, Foad Farhani^{a*}, Hassan Ali Ozgoli^b and Seyyed Mostafa Hosseinalipour^c

^aDepartment of Mechanical Engineering, Iranian Research Organization for Science and Technology, Tehran, 3313193685, Iran

^bSchool of Engineering, Macquarie University, Sydney, 2109, Australia

^cMechanical Engineering Department, Iran University of Science and Technology, Tehran, 1684613114, Iran

Article info:
Article history:

Received: 00/00/0000

Revised: 00/00/0018

Accepted: 00/00/0000

Online: 00/00/0000

Keywords:

CFD,

Ingress flow,

Rim cavity,

Secondary air system,

Test rig.

***Corresponding author:**f.farhani@irost.ir

Abstract

Hot gas ingestion, due to pressure differences in the turbine's main flow path, is a challenge for gas turbine designers. It reduces aerodynamic performance, increases temperature gradients and thermal stresses, and decreases disk life. Designers should predict the ingestion and use the precise design of the cooling system, balancing the cooling and sealing flow, to enable the turbine to operate at higher temperatures and efficiency to save costs and reduce harmful effects on turbine components. This paper presents a numerical investigation of a 1.5-stage test rig to study the ingestion phenomenon. A numerical tool was developed to enhance the coefficients and constants of a rapid ingestion model in a zero-dimensional secondary air system code applicable to power plant turbines, such as Frame 9. Comparisons of CFD and test results demonstrate satisfactory agreement. Combining CFD and experimental validation, a numerical effectiveness map for the selected test rig rim seal is presented. CFD results post-processing reveal that an increased cooling flow rate increases the pressure within the wheelspace, reduces swirl in the core region, and improves seal effectiveness. The swirl ratio was highly sensitive to SAS flow, increasing by 90% with a 50% reduction in SAS flow at a dimensionless radius of 0.85. Analysis of flow vectors exiting the axial clearance rim seal indicates that increasing the SAS flow rate enhances the main gas path flow disturbances. Moreover, at a constant flow rate, an increase in the first wheelspace flow rate increases the effectiveness of the second wheelspace by approximately 33%.

1. Introduction

Many analytical, experimental, and numerical studies have focused on the cooling process of gas turbine disks, including rotor-stator cavities,

to develop and improve the cooling performance of turbines. The rotor-stator system/structure is typical in the gas turbines' secondary air systems. The cavity formed in the space between the stationary and rotating disk is called the

wheel-space (WS). As expected, a boundary layer will form on the disk surface, and the radial downward flow on the stator supplies the boundary layer flow of the rotor. Based on experimental observations, the flow between a rotating and a stationary disk is classified as Batchelor flow, whereas the flow structure on the free disk is categorized as Stewartson flow [1].

Batchelor's 1951 model describes the flow between a stationary and a rotating disk as characterized by a central core of fluid. This core rotates with an angular velocity between zero and the rotor's angular velocity, Ω . The formation of this core is associated with two boundary layers: one on the rotating disk, analogous to that of a free disk, and another on the stationary disk. Within the stator's boundary layer, fluid flows radially inward; subsequently moving towards the rotating core.

Finally, this core flow is drawn into the rotor's boundary layer and expelled from the system [1]. Unlike the Batchelor model, Stewartson's 1953 approach [2] suggests that a boundary layer appears solely on the rotating disk, mirroring the free disk scenario. Stewartson's key conclusion was that the tangential velocity diminishes from $r\Omega$ on the rotor to zero on the stator, leading to his assumption that neither a stator boundary layer nor a central core is present [1].

Picha and Eckert's subsequent investigations in 1958 demonstrated that the presence or absence of shrouds significantly influenced core rotation. They reported no significant core rotation in open disk systems but observed its occurrence when the disks were shrouded, resembling typical rotor-stator configurations. Moreover, their work indicated an inverse relationship between the parameter G and the angular velocity ω of the core for a given rotor speed Ω [1].

Ingestion takes place when the pressure of the main flow near the seal exceeds the pressure within the wheel-space, the area between the rotor and stator disks. When this pressure differential exists, external fluid is ingested into the system. This ingested flow then moves radially inward, passing through the boundary layer on the stator before being conveyed axially into the rotating core. Subsequently, this flow

becomes entrained into the rotor's boundary layer and mixes with the superposed sealant flow, which enters the system through the center of the stationary disk.

Ultimately, the combined flow of the sealant and the ingested fluid exits the wheel-space through the seal clearance. Due to ingestion from the outside stationary environment, the flow structure changes; the core rotation decreases, and the moment on the disk surface increases. The transition from Batchelor to Stewartson flow is possible in large-clearance systems. The flow is much more complex here than a closed and confined system. The moment coefficient can increase from a value lower than the free disk to a value higher than the free disk [1].

Ingestion is always generated due to the pressure difference between the main flow and the wheel-space; however, different factors create this pressure difference. The flow through stationary vanes and moving blades creates an unsteady asymmetric pressure distribution. This factor produces *externally induced (EI)* ingestion in places where the primary gas flow pressure exceeds the wheel-space pressure [3].

The rotor disk is another factor that creates a pressure difference. When the disk rotates radially, it establishes a radial pressure gradient that exerts a centrifugal force (in the radial direction and outward) on the fluid. The pressure gradient resulting from rotation causes the wheel-space pressure to be lower than the primary flow pressure, causing fluid to enter the wheel-space. This is called *Rotationally-induced (RI) ingestion*. Hot gas can be ingested in the wheel-space under a combination of the mentioned factors, called combined ingestion (CI) [4].

Chew *et al.* [5] have presented an excellent review of the research conducted on the rim seal. Experimental data obtained from well-designed turbine test rigs can be used to validate computational fluid dynamics (CFD) simulations and refine theoretical models for turbine performance.

Several leading institutions, including Aachen University [6], the University of Arizona [7], the University of Sussex [8], General Electric [9], the University of Pennsylvania [10], and Bath University [11, 12], have developed specialized

test facilities to investigate ingestion-based flow phenomena.

CFD has become an indispensable tool for the detailed design of secondary air systems. It enables evaluating and selecting optimal solutions within various components, clearly visualizing the underlying flow physics.

Mirzamoghadam *et al.* [13] employed steady-state modeling to investigate the interaction between the main flow and cavity flow and the influence of vane fillets on the ingestion in HP turbine sections. The Spalart-Allmaras turbulence model was used in their research. Three distinct flow rates were considered. The steady-state modeling successfully predicted the ingress's oscillatory movement and penetration depth with varying purge flow rates.

Liu *et al.* [14] numerically simulated the flow field within a test rig's rim seal and WS at the University of Bath using the SST turbulence model and the Navier-Stokes equations. The simulation results were validated against experimental data. They reported that steady-state RANS simulations, considering rotor rotation but neglecting blade details, accurately predicted the swirl in the WS, except in regions very close to the rim seal.

Soghe *et al.* [15] conducted a numerical simulation of hot gas ingestion through a rim seal. Turbulence was modeled through the $k - \omega$ SST turbulence model. They compared the results with experimental data from a single-stage test rig at the University of Bath. The results demonstrate that the numerical solution of the steady-state Navier-Stokes equations can accurately predict RI ingestion and the aerothermal field within the WS.

Lalwani *et al.* [16] leveraged the commercial solver ANSYS CFX to investigate ingestion in both double and single-fin radial seals. The steady RANS equations and the shear stress transport (SST) turbulence model were used for the computations. This study introduces a 3D steady-state model as a practical tool for designers. Particularly in limited testing scenarios, this tool offers satisfactory qualitative predictions of the flow structure and provides a quantitative understanding of seal performance. The selection of an appropriate turbulence model is crucial for accurate CFD simulations of

ingestion in gas turbine rim seals. While various models are available, the complex flow physics involved often necessitates careful consideration of each model's strengths and weaknesses.

Alinejad *et al.* [17] successfully employed a standard $k-\varepsilon$ turbulence model to optimize the shape of the rotor using two different geometries. Also, in reference [18], a computational model with the $k-\varepsilon$ turbulence model and wall function has been used to investigate the effect of volute spread angle on efficiency, performance, and flow pattern inside the volute of squirrel cage fan. The SST turbulence model, selected for ingestion computations in this paper, is supported by the findings of mentioned papers. The SST model offers a good compromise between accuracy and computing cost [16].

The increasing demand for reduced energy consumption and the widespread use of gas turbines have driven significant research efforts to enhance the understanding, improve efficiency, upgrade existing systems, and develop infrastructure for optimal turbine design. Numerous studies have been conducted on modeling ingestion phenomena, but many questions remain regarding the behavior and performance prediction of secondary air system elements under these conditions. This paper presents a numerical approach for simulating ingress flow within a gas turbine rim seal.

Utilizing ANSYS CFX19.3, a detailed computational model was developed and validated against experimental data from a 1.5-stage test facility at Bath University. By reconstructing the geometry and mesh, boundary conditions consistent with the selected test rig were applied. A subsequent step involved investigating the flow behavior and the trend of changes in several key parameters after validating the developed model and comparing the numerical results with the available test rig data. The developed tool can be applied to model ingestion flow and extract performance curves for rim seals in other turbines.

2. Selected test rig

To validate the numerical model, a 1.5-stage axial turbine installed at Bath University is used

(Fig. 1). The blade arrangement is (stationary, moving, stationary), and the two stationary stages (stators) are separated by a rotating disk (rotor), creating two separate wheelspaces. The entry of sealing flow differs between the upstream and downstream wheelspaces. In the upstream region, the flow enters from the center of the stationary disk, whereas in the downstream region, entry occurs at two radial positions on one side of the seal. In both scenarios, the flow then proceeds radially outward within the wheelpace and ultimately mixes with the flow in the external annulus via the rim seal. This project, supported by Siemens, focuses on modeling the leakage flow from the nozzle and the inner carrier ring gap specifically in the upstream wheelpace.

Scobie [11] designed this equipment, and Patinios built it in 2015. Also, in 2020, Hualca [19] modified and upgraded the equipment through new experiments and further studies. This equipment can measure the effects of the rotor blades on the ingestion phenomenon.

2.1. Test rig operating conditions

The experimental test facility is designed to operate at two distinct design points, corresponding to rotational speeds of 3000 and 4000 (rpm). The number of vane-blade-vane is 32, 48, and 32, respectively, with 12 (mm) separations between each airfoil. The dimensioned cross-section of the test facility is shown in Fig. 2. For each design point, geometrically similar velocity triangles are considered to ensure the same nondimensional driving potential, ΔC_p , in the annulus for the different rotational speeds.

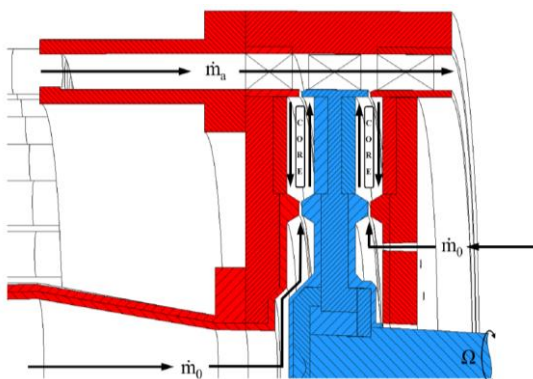


Fig. 1. Bath University 1.5-stage experimental test facility, blue: rotating and red: stationary part [11].

The ratio of axial to rotational Reynolds numbers gives the flow coefficient ($CF = Re_w / Re_\phi$). Considering the design of current industrial gas turbines and ensuring sufficient potential for externally induced flow, the target flow coefficient is 0.4, which approximately matches the average value in the first 10% of the span in the Siemens gas turbine engine design. To meet the target flow coefficient, a compressor with a 1.5 kg/s mass flow rate capacity is installed. The characteristic radius is $b = 190$ (mm). The annulus height is considered to be 25 (mm), resulting in a hub-to-tip ratio (R_i / R_o) of 0.89. More details regarding the test rig are provided in references [11] and [19].

3. Reconstruction of the 1.5-stage test rig geometry

The numerical model geometry was divided into the primary and secondary flow paths. The secondary air flow path encompasses the flow within the upstream and downstream wheelspaces. A mixture of air and tracer gas CO₂ was supplied at the inlet of these sections. This mixture was modeled as a multicomponent flow within CFX, meaning the air and CO₂ were treated as fully mixed at the molecular level, sharing the same velocity, pressure, and temperature fields.

Mass transfer between the components was calculated using both convective and diffusive transport models within CFX. This approach accounts for the distinct physical properties of each component and calculates appropriate mixture-averaged properties for each control volume based on the local concentration of each species. Sutherland's law is used to calculate the dynamic viscosity and thermal conductivity. Using data from a cross-section [11], a 3D model of each wheelpace was reconstructed using Gambit and ANSYS SpaceClaim software. The geometry and the generated mesh are depicted in Fig. 3.

The main flow path encompasses the first stationary and moving blades and the second stationary blade. Using the GetData Graph Digitizer software, the coordinates of the blade profile cross-sections were extracted. Subsequently, the extracted data was converted into a suitable format for meshing the geometry in TurboGrid using BladeGen. The geometry of the blades located in the main flow path and a sample mesh is presented in Figs. 4-6.

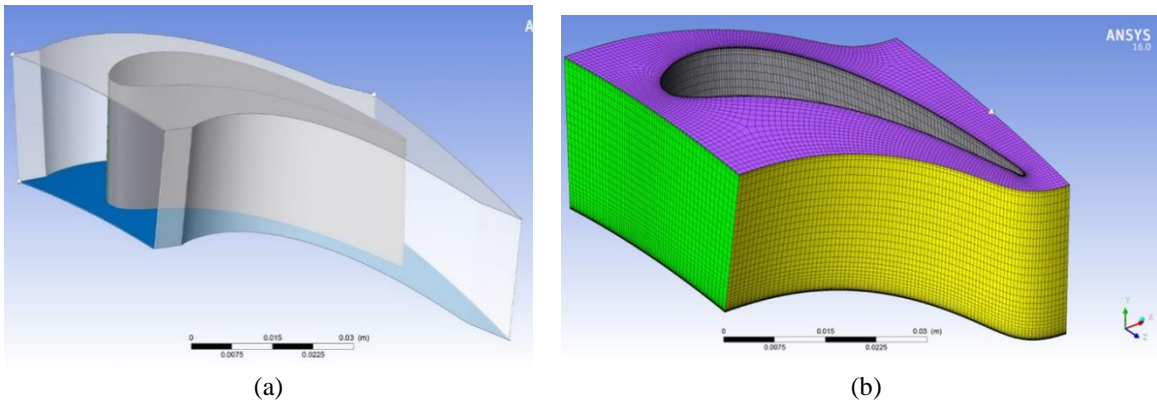


Fig. 4. The first vane: (a) geometry and (b) a generated grid.

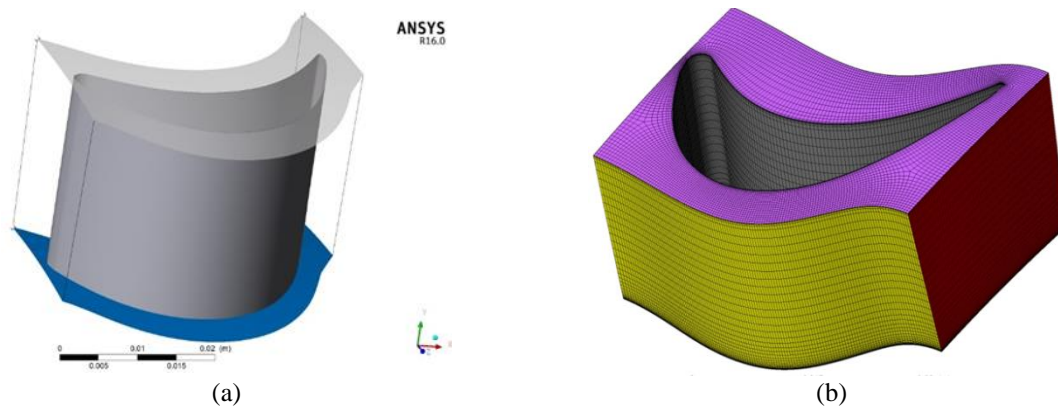


Fig. 5. The first blade: (a) geometry and (b) a generated grid.

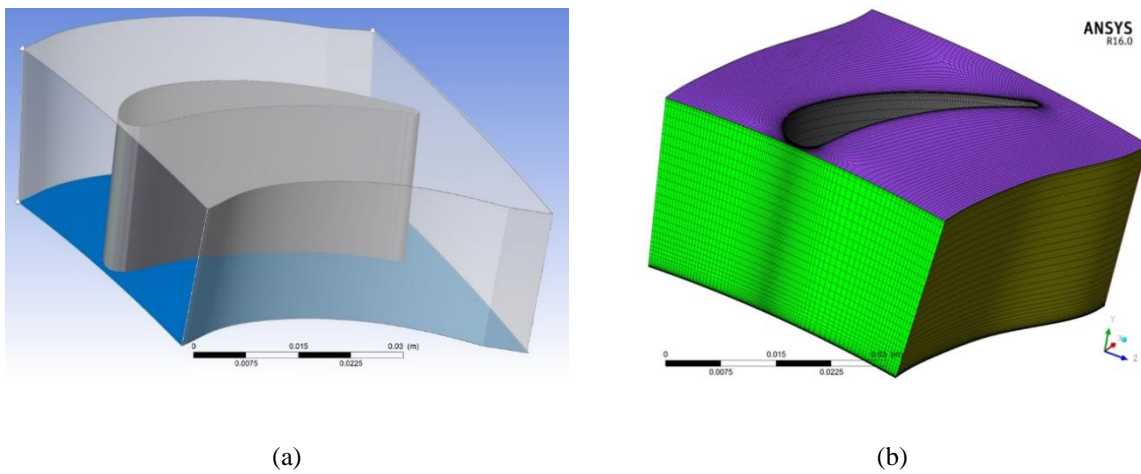


Fig. 6. The second vane: (a) geometry and (b) a generated grid.

3.1. Applied boundary conditions

The 3D model is presented in Fig. 7, in which the blue domain corresponds to the first and second wheelspaces, and the red domains represent the

main gas flow path. The computational domain for the flow in the first and second nozzles is stationary, and the computational domain for the first moving blade and the first and second wheelspaces is considered rotating.

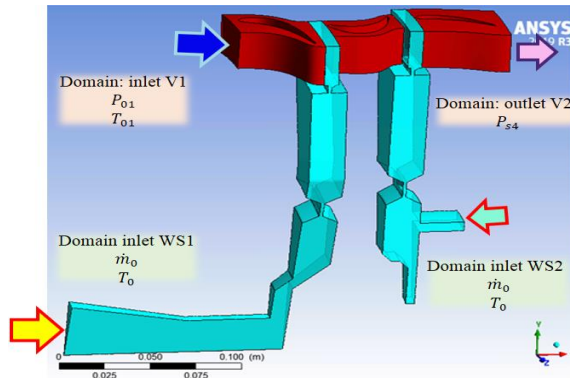


Fig. 7. Visualization of the main flow and SAS domains.

The interfaces between the first nozzle and the first wheelpace and between the second wheelpace and the second nozzle are defined as Frozen Rotor. Also, the interface between the first moving blade and the first and second wheelspaces is defined as General Connection (Stage). The angle corresponding to the desired domain sectors is also entered: 11.25 degrees for the first and second nozzles and wheelspaces, and 7.5 degrees for the first moving blade. The performance of the 1.5-stage test rig was evaluated using boundary conditions extracted from data and information presented in references [11] and [19], the main details of which are summarized in Table 1.

The rotor was designed for a 6000 (rpm) speed, but flow rate limitations and maximum allowable rotational speed, consequently affecting the rotational Reynolds number, restricted the operation to 4000 (rpm). The flow coefficient during the tests was $C_F = 0.34$. According to Table 1, at 4000 (rpm), the axial Reynolds number and the exit Mach number from the second stationary blade are 0.37. Tracer gas with a concentration of 3% was seeded at the inlet between the upstream and downstream wheelspaces.

Table 1. Operating conditions of the 1.5-stage test rig of the University of Bath [22].

| Parameters | Value | |
|---------------------------------------|-------------------|-------------------|
| Disc speed (rpm) | 3000 | 4000 |
| Rotational Reynolds number, Re_ϕ | 7.2×10^5 | 1×10^6 |
| Axial Reynolds number, Re_w | 2.4×10^5 | 3.4×10^5 |
| Mach number at vane exit, M | 0.28 | 0.37 |
| Flow coefficient, C_F | 0.34 | |

The boundary conditions used in the numerical modeling were total pressure, P_{01} and total temperature, T_{01} at the inlet of the first stator, static pressure P_{s4} at the outlet of the second stator, and the mass flow rate \dot{m}_0 and total temperature T_0 at the inlet of the first and second wheelspaces. Values of the total pressure, temperature, and mass flow rate at the inlet boundaries were adjusted based on the available geometric information and data. By varying the static pressure at the outlet, the axial Reynolds number and Mach number at the outlet of the second stator were calculated. An iterative process continued until the axial Reynolds numbers matched the values presented in Table 1.

The extraction and evaluation of the results of the numerical simulations were performed after ensuring convergence. This was achieved by verifying three criteria: examining the residuals, monitoring several key variables obtained from the solution, and analyzing the trends and imbalances in the computational domain, as described in [20].

4. Grid sensitivity analysis

Grid generation can directly affect the results of numerical solutions; this issue highlights the importance of investigating and analyzing the insensitivity of the results to the generated grid. For boundary layer (B.L.) generation, the distance of the first cell from the wall, the growth ratio (G.R.), the number of layers, and the final thickness of the boundary layer were considered. The first effective parameter (the distance of the first cell from the wall) was determined based on the selected turbulence model.

Given the selection of the $k - \omega$ SST model and the ANSYS-CFX solver's ability to automatically switch between $LR k - \omega$ SST and $HR k - \omega$ SST modes based on the generated mesh; however, efforts have been made to optimize the generated mesh as much as possible. Therefore, in the vicinity of walls with lower physical sensitivity, more nodes adjacent to the wall were placed in the logarithmic region, and a coarser grid was used. Considering the geometry and flow behavior, the grid distribution was denser in domain regions with

higher physical sensitivity, and the first node was closer to the wall.

To this end, in the first step, the distance of the first node was estimated using Eq. (1), in which Δy is the distance between the wall and the first node, L is the length scale of the flow, y^+ represents the desired value of y^+ , and Re_L is the Reynolds number based on the length scale, L [20].

$$\Delta y = Ly^+ \sqrt{74} Re_L^{-\frac{13}{14}} \quad (1)$$

Five meshes were generated within the specified geometry to investigate the sensitivity of the numerical model to mesh density. The first to fifth meshes comprised approximately 1.46, 2.63, 10.96, 11.458, and 22.8 million elements, respectively. Through careful mesh generation, even the coarser meshes exhibited desirable mesh quality characteristics, such as proper element distribution and adequate first cell height near walls. The element count for individually assembled model components is presented in Table 2, with detailed meshing information for the first wheel-space provided in Table 3.

4.2. Grids sensitivity analysis results

A plot of critical parameters obtained from the Computational Fluid Dynamics simulation, such as mass flow rate and temperature, against the number of elements in each mesh is typically created to demonstrate the independence of the

CFD results from the mesh. When the values of these parameters become relatively insensitive to further mesh refinement, i.e., less than a 5% change with additional refinement, the mesh is considered sufficiently acceptable. However, this threshold may be adjusted depending on the specific problem and desired accuracy.

Fig. 8 illustrates the variation of mass flow rate with the number of elements for the modeled test stand. Despite a significant difference in the number of elements between the coarsest mesh (1.46 million elements) and the finest mesh (22.8 million elements), the mass flow rate varies by only 4.57%. One of the key factors contributing to this accuracy is the proper placement of the first node of the mesh at an appropriate distance from the walls in all meshes. This highlights the importance of the y^+ parameter in ingestion simulations.

The sealing effectiveness is defined as $\epsilon_c = (c_s - c_a)/(c_0 - c_a)$, where c_0 , c_a and c_s are the concentration of carbon dioxide gas at the inlet of the wheel-space, annulus, and stationary wall in the investigated radius, respectively. In this analysis, in addition to the flow rate, a diagram of the effectiveness at a dimensionless radius of 0.958 in WS1 is also plotted against the number of mesh elements in Fig. 9. The maximum effectiveness difference in the mesh analysis is about 6%, which decreased to less than 2.3% in the last two meshes. Given the computational speed and cost, this study selected the fourth mesh with 11,458,059 elements as the final mesh.

Table 2. The number of elements in the grid sensitivity analysis.

| Case | First vane | First blade | Second vane | First wheel-space | Second wheel-space |
|------|------------|-------------|-------------|-------------------|--------------------|
| 1 | 391394 | 171990 | 234894 | 391394 | 347964 |
| 2 | 635740 | 286892 | 502200 | 635740 | 584633 |
| 3 | 1787442 | 925994 | 1083425 | 1787442 | 1664585 |
| 4 | 3239487 | 2111670 | 2255580 | 3239487 | 2158476 |
| 5 | 4215312 | 3773952 | 5280876 | 5461896 | 4039241 |

Table 3. Statistical characteristics of grids generated for 1st wheel-space.

| Case | No. of elements | B.L. wedges | Layers in | G.R. |
|------|-----------------|-------------|-----------|------|
| 1 | 391394 | 165838 | 15 | 1.35 |
| 2 | 635740 | 316234 | 20 | 1.2 |
| 3 | 1787442 | 898123 | 25 | 1.18 |
| 4 | 3239487 | 1897262 | 30 | 1.15 |
| 5 | 5461896 | 3325506 | 35 | 1.12 |

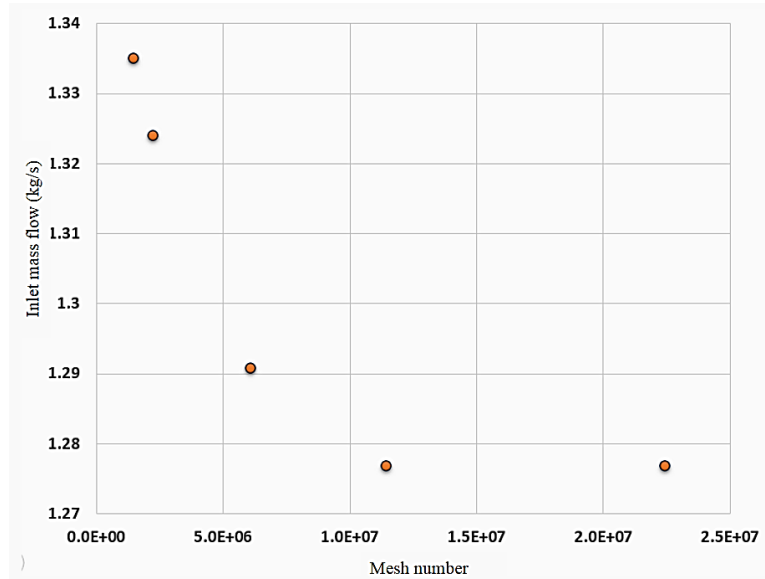


Fig. 8. Variation of 1st vane inlet mass flow vs. number of mesh elements.

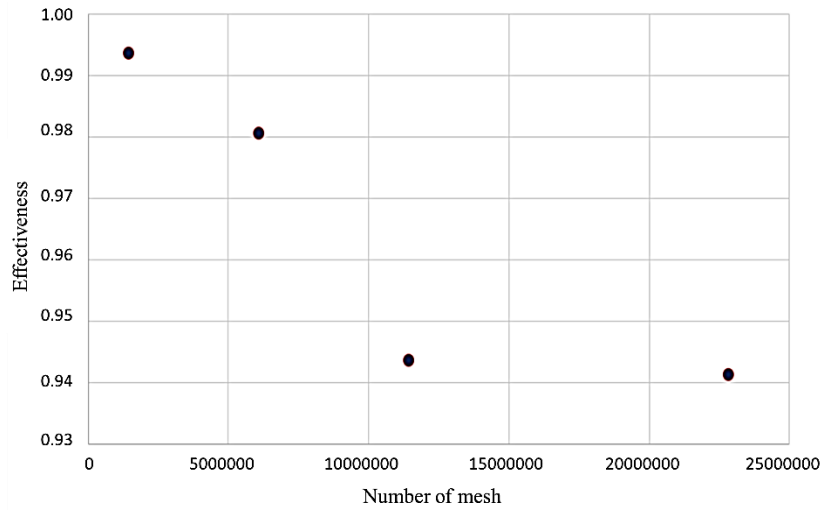


Fig. 9. Variation of 1st wheelspace effectiveness vs. number of mesh elements.

5. Results and discussion

The sensor locations in the test rig and lines coinciding with points on the hub of stationary vanes (A1, A2, and A3) were created in CFD-Post, as shown in Fig. 10.

5.1. Pressure measurement in the annulus

Steady-state pressure measurements were conducted at the pitch of each stationary blade (11.25 degrees). Upstream and downstream pressures were recorded using two independent sets of 15 pressure gauges (each with a diameter

of 0.5 mm) mounted on the end walls corresponding to A_1 and A_3 . Upstream pressure gauges were positioned on a stationary platform 2.5 mm from the first vane. Downstream pressure gauges were embedded 1.5 mm axially from the downstream rim seal. The pressure coefficient, $C_{p,a}$ is defined as Eq. (2):

$$C_{p,a} = \frac{(p_a - \bar{p}_a)}{\frac{1}{2\rho\Omega^2 b^2}} \quad (2)$$

where p_a is the static pressure and \bar{p}_a is the average pressure at the blade pitch. The

circumferential variations of the steady pressure coefficient over two nondimensional vane pitches (θ) at locations A1 and A3 are shown in Fig. 11. The measurements in Fig. 11 were conducted at a flow coefficient, and the obtained results were independent of Re_ϕ and can be said to be independent of the rotational speed. Reference [19] mentions that other rotational speeds were also tested, but the corresponding results were not presented. A comparison of the dimensionless pressure distribution obtained at location A1 from the computational domain under consideration is given in Fig. 11. As can be seen, the trend of change and the predicted behavior for the parameter under consideration in the numerical solution is suitable and acceptable compared to the experimental results.

Fig. 12 compares the dimensionless pressure distribution at the trailing edge of the first vane in two positions, A1 and A2, based on the numerical model. As can be seen in this figure, as the flow moves downstream, the difference between the maximum and minimum dimensionless pressure ($\Delta C_{p,a}$) decreases. This decreasing trend in the studied parameter has also been mentioned by Patinios *et al.* 0.

5.2. Analysis of seal effectiveness

The effectiveness of the seal, obtained from the numerical solution, is compared with the digitized values from Hualka [19] in Fig. 13. As expected, the effectiveness is maximum inside the wheelspace and minimum in the main flow path.

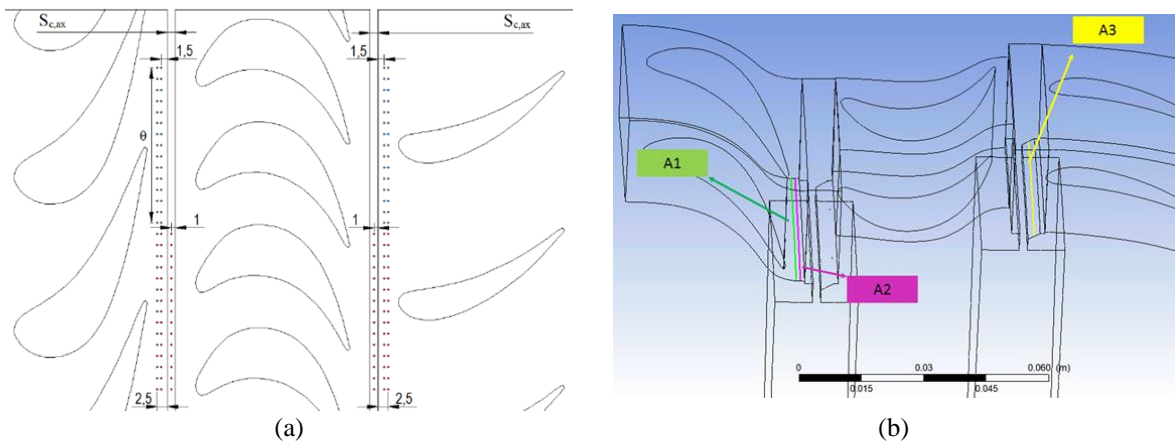


Fig. 10. (a) Location of test rig sensors [19] and (b) generated lines in the computational domain.

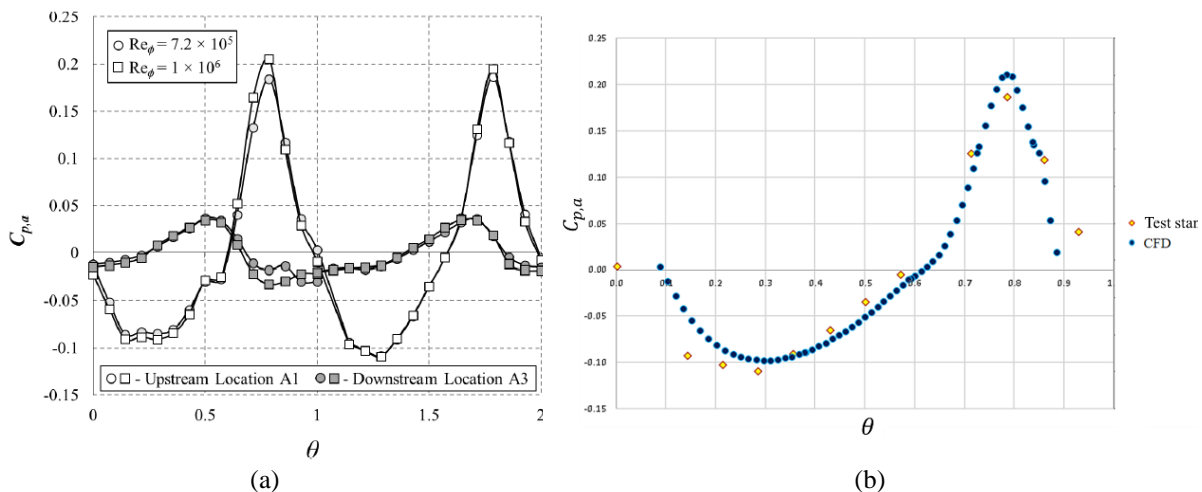


Fig. 11. (a) Circumferential distribution of $C_{p,a}$ over two non-dimensional vane pitches [22] and (b) comparison of CFD and test stand pressure coefficient distribution over one vane pitch at location A1.

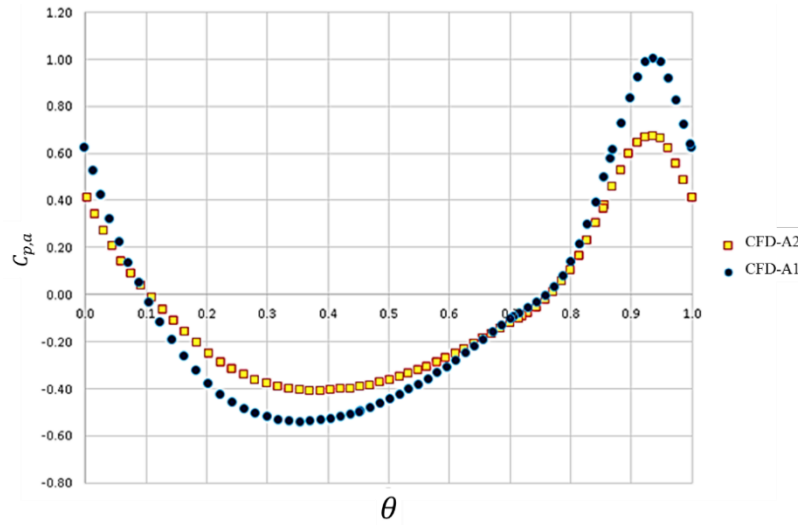


Fig. 12. Comparison of the distribution of $C_{p,a}$ over non-dimensional vane pitch at locations A1 and A2 in the numerical model.

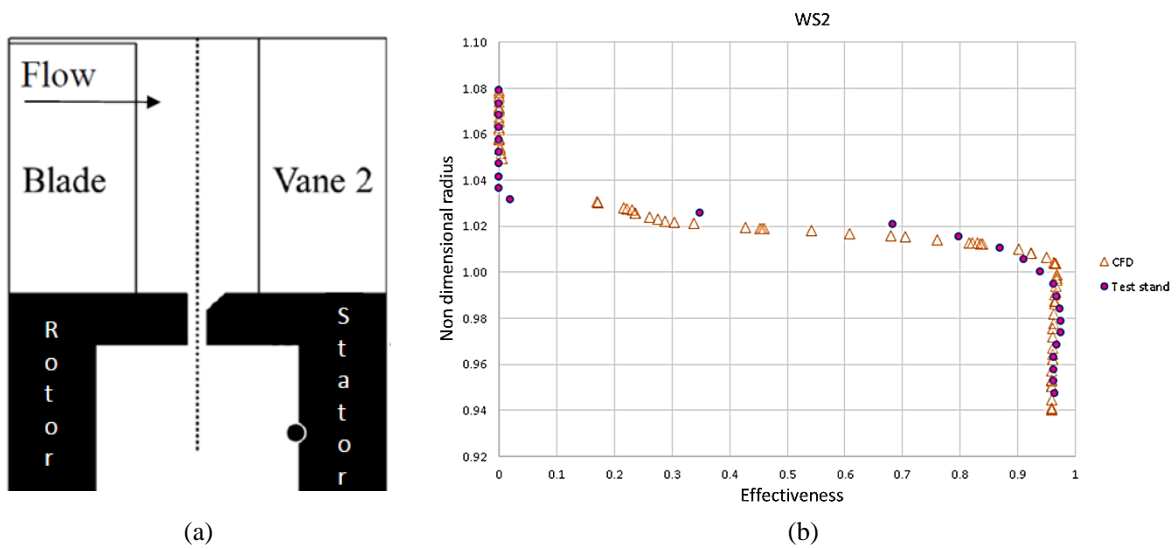


Fig. 13. (a) Mid plane at 2nd WS seal and (b) comparison of radial variation of CFD and test stand effectiveness [19].

The region between the maximum and minimum effectiveness is the mixing zone of the main gas flow and the secondary flow. The test stand results show more ingress flow than the numerical solution. However, a reasonable agreement between the obtained results is observed.

5.3. Flow analysis in the numerical model

The flow parameters within the computational domain were investigated, and a sample of these

is presented here to analyze and better understand the ingestion phenomenon. For this purpose, a range of different operating conditions was created by varying the mass flow rate supplied into the inlet channels of the secondary airflow in the first and second wheelspaces while keeping the other parameters presented in Table 1 constant. The selection of the applied boundary conditions is given in Table 4.

Table 4. Boundary conditions of the numerical model.

| Case | Rotational speed (rpm) | Re_ϕ | Re_w | C_F | Mass flow (gr/s) | |
|------|------------------------|-------------------|-------------------|-------|------------------|-----------------|
| | | | | | WS ₁ | WS ₂ |
| 1 | 3000 | 7.2×10^5 | 2.4×10^5 | 0.34 | 70 | 70 |
| 2 | 3000 | 7.2×10^5 | 2.4×10^5 | 0.34 | 50 | 50 |
| 3 | 3000 | 7.2×10^5 | 2.4×10^5 | 0.34 | 30 | 30 |
| 4 | 3000 | 7.2×10^5 | 2.4×10^5 | 0.34 | 10 | 10 |
| 5 | 3000 | 7.2×10^5 | 2.4×10^5 | 0.34 | 6 | 6 |
| 6 | 3000 | 7.2×10^5 | 2.4×10^5 | 0.34 | 2 | 2 |
| 7 | 3000 | 7.2×10^5 | 2.4×10^5 | 0.34 | 35 | 7 |
| 8 | 4000 | 1.0×10^6 | 3.4×10^5 | 0.34 | 70 | 70 |
| 9 | 4000 | 1.0×10^6 | 3.4×10^5 | 0.34 | 40 | 40 |

5.4. Analysis of the main and secondary flow interaction

Contours of Mach number in the stationary frame and flow vectors in the space between the 1st vane and the WS1 for two nondimensional seal flow rates, $\Phi_0 = 0,003$ and $\Phi_0 = 0,21$, are shown in Fig. 14 and 15, respectively. Here ϕ_0 is defined as $(C_{w,0} / 2\pi G_c Re_\phi)$, where $C_{w,0} = \dot{m} / \mu b$, G_c , b , and μ are the seal-clearance ratio, the characteristic radius of the seal, and dynamic viscosity, respectively. As expected, the minimum Mach number and maximum static exit pressure occur at the trailing edge of the stationary vane.

Additionally, with an increase in the nondimensional flow rate supplied at the WS1 inlet, the flow vectors in the main gas flow path, as shown in Fig. 15, deviate significantly from their original path. This causes disturbances at the mixing location of the two flows.

The velocity distribution in a section of the first wheel-space for two different seal flow rates is depicted in Fig. 16. As observed, the egress of SAS flow from the cavity into the primary airflow path causes blockage in the annulus. The geometry of the modeled rim seal is axial clearance type; the flow exiting this seal has a cross-flow pattern relative to the main gas flow, which can lead to higher aerodynamic losses.

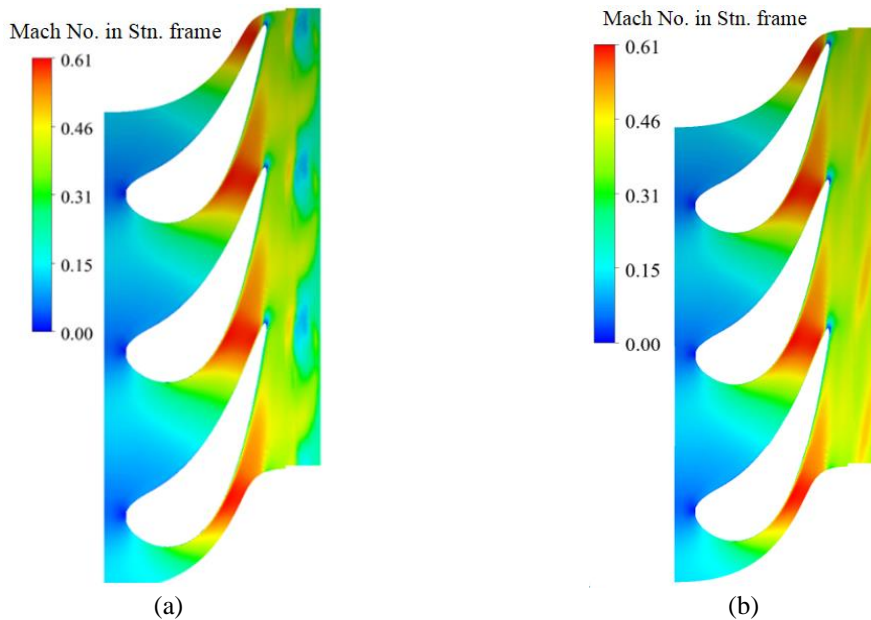


Fig. 14. Distribution of Mach No. in a plane close to the hub (a) $\Phi_0 = 0.21$ and (b) $\Phi_0 = 0.003$.

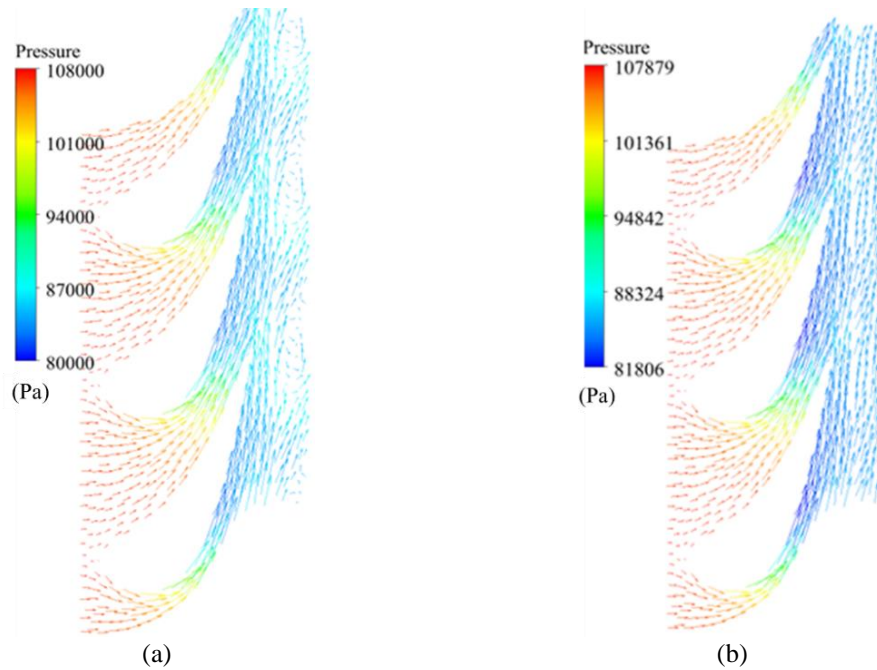


Fig. 15. Flow vector in a plane close to the hub: (a) $\Phi_0 = 0.21$ and (b) $\Phi_0 = 0.003$.

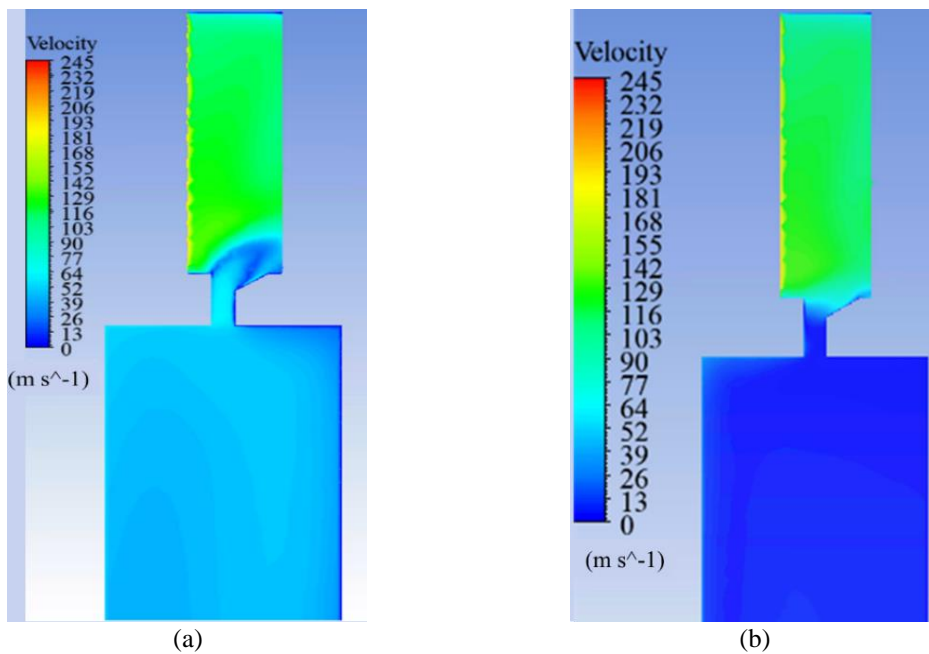


Fig. 16. Distribution of velocity in a cross-section: (a) $\Phi_0 = 0.21$, (b) $\Phi_0 = 0.003$.

Furthermore, as the engine operating conditions become more realistic, it is predicted that the numerical modeling of ingestion in a geometry with an axial clearance seal will be much more complex, and the selection of turbulence models will be very challenging. The concentration distribution in a plane near the hub, for a nondimensional flow rate of 0.003, is shown in

Fig. 17. According to the results, the tracer gas concentration seeded into the wheelspace is highest at the exit of the rim seal and between the two vanes' pitch. With an increase in the nondimensional supplied flow rate, the concentration value increases significantly, as shown in **Fig. 18**.

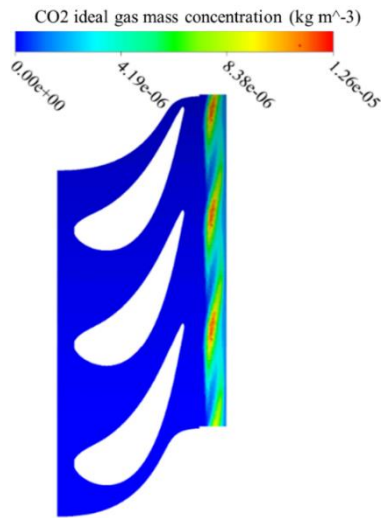


Fig. 17. Distribution of CO₂ concentration in a plane close to the hub for $\Phi_0 = 0.003$.



Fig. 18. Distribution of CO₂ concentration in a plane close to the hub: (a) $\Phi_0 = 0.21$ and (b) $\Phi_0 = 0.003$.

5.5. Flow in wheelspace

As expected, with an increase in the supplied flow rate into the wheelspace, this part of the domain becomes pressurized, as shown in Fig. 19. The increase in wheelspace pressure leads to a decrease in core rotation. Decreasing the SAS mass flow rate (from 20 to 10 (g/s)) increased the swirl ratio (approximately 90%) at the dimensionless radius of 0.85. The radial variation of the swirl ratio (β) in the first wheelspace is presented in Fig. 20. With an increase in the radius and distance from the wheelspace core, the swirl ratio increases due to the ingestion of the annulus flow into the wheelspace and its mixing with the wheelspace flow.

The radial distribution of effectiveness in this part of the domain also confirms the occurrence of ingestion, as shown in Fig. 21. For the condition with a zero nondimensional flow rate, a significant portion of the wheelspace is filled with the ingress flow from the annulus, and therefore, the CO₂ concentration in this space is minimal; and the seal effectiveness in this condition is zero.

As presented in Fig. 19, with an increase in the ingress flow rate into the wheelspace, this part of the domain becomes pressurized, thus reducing the amount of ingress flow and consequently increasing the seal effectiveness and the CO₂ concentration. For a nondimensional flow rate of 0.29, the seal effectiveness is close to 1, which means that ingestion is prevented in this region, as shown in Fig. 21.

To further investigate and to extract the effectiveness-dimensionless sealing parameter diagram for the numerical results, the seal effectiveness was calculated at $r/b = 0.958$. The resulting diagram is shown in Fig. 22. As expected and consistent with the observations described above, the seal effectiveness is zero at zero flow rate. As the dimensionless sealing parameter increases, the seal effectiveness also increases. At a dimensionless flow rate of 0.29, the seal effectiveness approaches its maximum value of 1 at the dimensionless radius under investigation. This indicates that at this flow rate, ingestion is effectively prevented, further confirming the findings presented in Fig. 21.

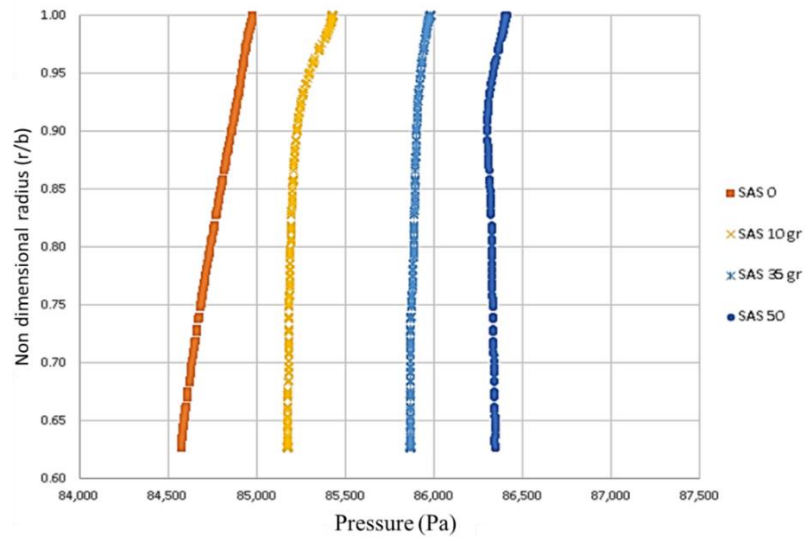


Fig. 19. Radial variation of pressure at different SAS flows.

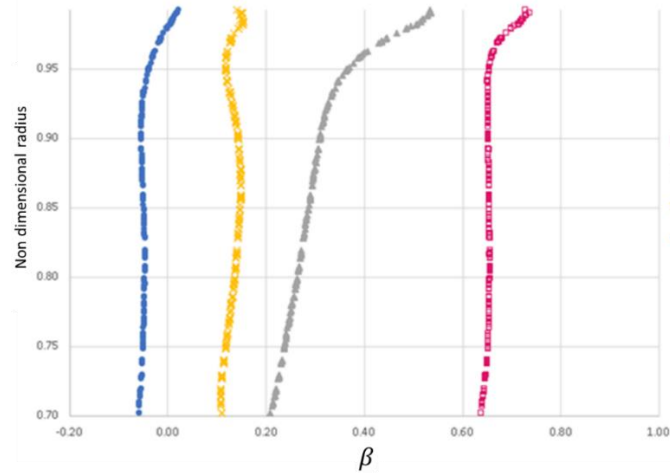


Fig. 20. Radial variation of swirl at different SAS flows.

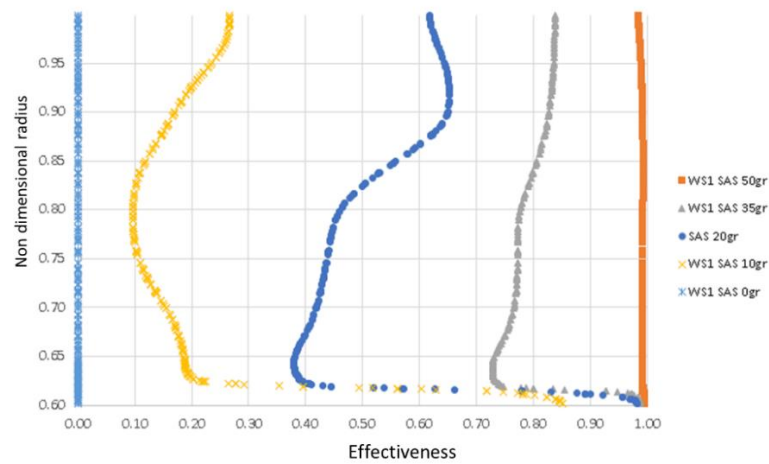


Fig. 21. Radial variation of effectiveness at different SAS flows.

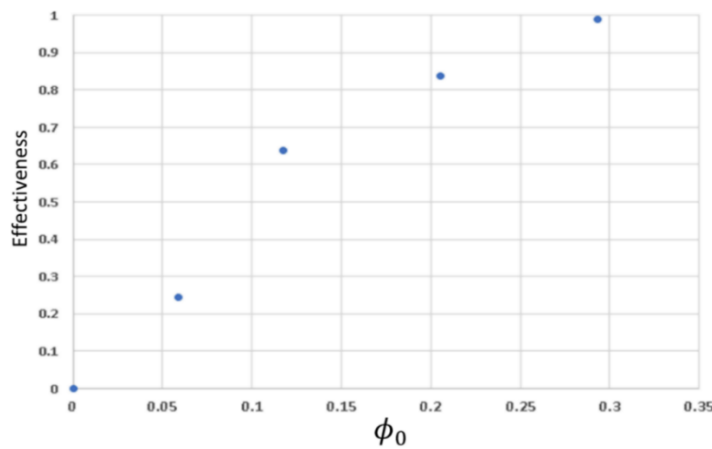


Fig. 22. Variation of 1st wheelspace effectiveness vs. nondimensional flow rate.

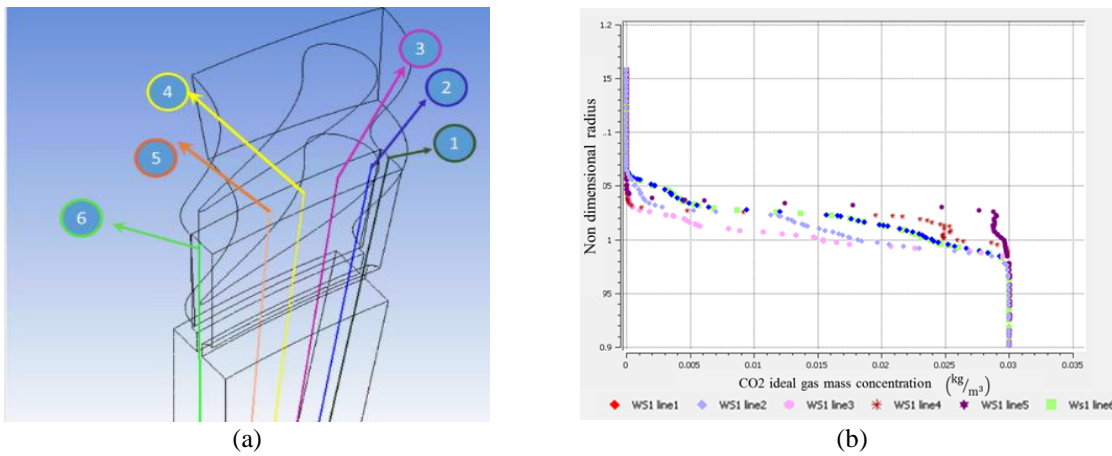


Fig. 23. (a) Position of lines in the middle of rim seal and (b) effectiveness at lines with various angles in lines of WS1 for $\phi_0 = 0,29$.

5.6. Circumferential distribution of effectiveness in the 1st wheelspace

Multiple lines were generated in the middle of the seal from the 1st wheelspace to investigate the circumferential distribution of effectiveness within the seal clearance. Fig. 23 presents the effectiveness distribution along each of these mid-seal lines for a nondimensional flow rate of $\phi_0 = 0.293$. As evident in Fig. 23, for nondimensional radii exceeding 0.97, a non-uniform effectiveness distribution is observed at various angles. This non-uniformity is attributed to the non-uniform pressure distribution in both the main flow and the flow exiting the wheelspace.

The circumferential effectiveness distribution for the mid-seal of the 2nd wheelspace was also

investigated, and a non-uniform distribution was observed. The downstream wheelspace exhibits notable distinctions compared to its upstream counterpart. Specifically, the axial flow within the annulus is directed from the rotor towards the stator, and the ingested fluid rotates in a direction opposite to that of the turbine disk.

Another noteworthy observation is that, for a constant flow rate from the second wheelspace, increasing the ingress flow rate in the upstream wheelspace positively impacted the downstream effectiveness, as shown in Table 5. This could be due to the re-ingestion of the upstream wheelspace flow into the second wheelspace, which requires further investigation and detailed modeling.

Table 5. Effect of increasing mass flow of upstream wheelspace on downstream.

| Case | ND mass flow Φ_0 | | CO ₂ concentration at $r/b = 0.958$ of WS ₂ |
|------|-----------------------|-----------------|---|
| | WS ₁ | WS ₂ | |
| 1 | 0.114 | 0.114 | 0.021 |
| 2 | 0.293 | 0.114 | 0.028 |

6. Conclusions

In this paper, a suitable numerical infrastructure capable of modeling the ingestion phenomenon was created using the 1.5-stage test rig at the University of Bath. The geometry in the main gas flow path includes the stator and rotor blades of the first stage and the stator blade of the second stage. Also, the secondary air flow path comprises the space between the first and second wheelspaces. All flow paths in the test rig were reconstructed and meshed. By post-processing the solutions obtained in this paper, the following results were obtained:

1. A reasonable agreement was achieved between the numerical simulation results and the available experimental data from the reference [19] in the evaluation and post-processing.
2. By increasing the SAS flow into the first wheelspace, the wheelspace became higher in pressure, and the core flow swirl decreased.
3. Furthermore, as the radius increases and moves away from the wheelspace core, the swirl ratio increases due to the ingestion of the annulus flow into the wheelspace and its mixing with the secondary airflow.
4. A 50% reduction in the SAS mass flow rate (from 20 to 10 g/s) led to a substantial 90% increase in the swirl ratio at the dimensionless radius of 0.85, indicating a strong influence of SAS flow on swirl characteristics.
5. A non-uniform distribution of effectiveness was observed in the middle of the rim seal clearance in both the first and second wheelspaces, which is caused by the non-uniform pressure distribution of the flow at the exit of the wheelspace and the main flow. As in reference 0 cited that the distribution of effectiveness across a vane pitch is dependent on the position (θ).
6. Another noteworthy observation is that, for a constant flow rate from the downstream wheelspace, increasing the supplied mass flow

rate in the upstream wheelspace, by a factor of 2.5, positively impacted the downstream effectiveness. The downstream effectiveness increased from 0.021 to 0.028, representing a 33% improvement.

Acknowledgment

The authors would like to express their sincere appreciation for the help and cooperation rendered by the TurboTec Company team. Their expertise and willingness to collaborate have been instrumental in the successful completion of this research.

References

- [1] J. M. Owen and R. H. Rogers, *Flow and Heat Transfer in Rotating Disc Systems, Vol. 1: Rotor-stator systems*, Research Studies Press Ltd, England, (1989).
- [2] K. Stewartson, "On the flow between two rotating coaxial disks", *Math. Proc. Cambridge Philos. Soc.*, Vol. 49, No. 2, pp. 333-341, (1953).
<https://doi.org/10.1017/S0305004100028437>
- [3] J. M. Owen, K. Zhou, O. Pountney, M. Wilson and G. Lock, "Prediction of Ingress Through Turbine Rim Seals-Part I: Externally Induced Ingress", *J. Turbomach.*, Vol. 134, No. 3, pp. 1-13, (2012).
<https://doi.org/10.1115/1.4003070>
- [4] J. M. Owen, "Prediction of ingestion through turbine rim seals-part I: Rotationally induced ingress", *J. Turbomach.*, Vol. 133, No. 3, pp. 1-9, (2011).
<https://doi.org/10.1115/1.4001177>

- [5] J. W. Chew, F. Gao and D. M. Palermo, "Flow mechanisms in axial turbine rim sealing", *Proc. Inst. Mech. Eng., Part C: J. Mech. Eng. Sci.*, Vol. 233, pp. 7637–7657, (2018).
<https://doi.org/10.1177/0954406218784612>
- [6] D. E. Bohn, A. Decker, M. Hongwei and M. Wolff, "Influence of sealing air mass flow on the velocity distribution in and inside the rim seal of the upstream cavity of a 1.5 stage turbine", *Proc. of ASME Turbo Expo*, Atlanta, Georgia, USA, (2003).
<https://doi.org/10.1115/GT2003-38459>
- [7] R. P. Roy, J. Feng, D. Narzary and R. E. Paolillo, "Experiment on gas ingestion through axial-flow turbine rim seals", *J. Eng. Gas Turbines Power*, Vol. 127, No. 3, pp. 573-582, (2005).
<https://doi.org/10.1115/1.1850499>
- [8] O. Gentilhomme, N. J. Hills, A. B. Turner and J. W. Chew, "Measurement and analysis of ingestion through a turbine rim seal", *J. Turbomach.*, Vol. 125, No. 3, pp. 505-512, (2003). <https://doi.org/10.1115/1.1556411>
- [9] P. Palafox, Z. Ding, J. Bailey, T. Vanduser, K. Kirtley, K. Moore and R. Chupp, "A new 1.5 stage turbine wheelspace hot gas ingestion rig - Part I: Experimental test vehicle, measurement capability and baseline results", *Proc. of ASME Turbo Expo*, San Antonio, Texas, USA, (2013).
<https://doi.org/10.1115/GT2013-96020>
- [10] M. Barringer, A. Coward, K. Clark, K. A. Thole, J. Schmitz, J. Wagner, M. A. Alvin, P. Burke and R. Dennis, "The design of a steady aero thermal research turbine for studying secondary flow leakages and airfoil heat transfer", *ASME Turbo Expo*, Düsseldorf, Germany, (2014).
<https://doi.org/10.1115/GT2014-25570>
- [11] J. Scobie, "An Experimental Study of Gas Turbine Rim Seals", PhD thesis, University of Bath, Dept. Mechanical Eng., London, (2014).
- [12] C. M. Sangan, "Measurement of Ingress Through Gas Turbine Rim Seals", PhD thesis, University of Bath, Dept. Mechanical Eng., London, (2011).
- [13] A. Mirzamoghdam, G. Heitland, M. Morris, J. Smoke, M. Malak and J. Howe, "3D CFD ingestion evaluation of a high pressure turbine rim seal disk cavity", *ASME Turbo Expo*, Berlin, Germany, (2008).
<https://doi.org/10.1115/GT2008-50531>
- [14] J. Liu, A. Weaver, T. Shih, C. Sangan and G. Lock, "Modelling and Simulation of Ingress into the Rim Seal and Wheelspace of a Gas-Turbine Rotor-Stator Configuration", in *53rd AIAA Aerospace Sciences Meeting*, Kissimmee, Florida, (2015).
<https://doi.org/10.2514/6.2015-1445>
- [15] R. D. Soghe, C. Bianchini, C. M. Sangan, J. A. Scobie and G. D. Lock, "Numerical characterization of hot gas ingestion through turbine", *Proc. of ASME Turbo Expo*, Seoul, South Korea, (2016).
<https://doi.org/10.1115/1.4034540>
- [16] Y. Lalwani, C. M. Sangan, M. Wilson and G. D. Lock, "Steady computations of ingress through gas turbine rim seals", *Proc. Inst. Mech. Eng., Part A: J. Power Energy*, Vol. 229, No. 1, pp. 2-15, (2015).
<https://doi.org/10.1177/0957650914552697>
- [17] J. Alinejad, N. Montazerin, S. Samarbakhsh, "Accretion of the efficiency of a forward-curved centrifugal fan by modification of the rotor geometry: computational and experimental study", *Int. J. Fluid Mech. Res.*, Vol. 40, No. 6, pp. 469-481, (2013).
- [18] S. Samarbakhsh, J. Alinejad, "Experimental and numerical analysis of eight different volutes with the same impeller in a squirrel-cage fan", *2nd European conference of Control and Mechanical Engineering*, (2011).

- [19] F. P. Hualca-Tigsilema, “An Experimental Study of Ingress Through Gas-Turbine Rim Seals”, PhD thesis, Dept. Mechanical Eng., University of Bath, London, (2020).
- [20] “ANSYS CFX-Solver Theory Guide”, Inc., ANSYS, (2014).
- [21] M. Patinios, J. A. Scobie, C. M. Sangan, J. M. Owen and G. D. Lock, “Measurements and Modeling of Ingress in a New 1.5 Stage Turbine Research Facility”, *J. Eng. Gas Turbines Power*, Vol. 139, pp. 012603, (2017). <https://doi.org/10.1115/1.4034240>
- [22] J. A. Scobie, C. M. Sangan, F. P. Hualca and G. D. Lock, “Egress interaction through turbine rim seals”, *Proc. of ASME Turbo Expo*, Charlotte, NC, USA, (2017). <https://doi.org/10.1115/GT2017-64632>